NANO LETTERS

Letter

pubs.acs.org/NanoLett

Midinfrared Plasmon-Enhanced Spectroscopy with Germanium Antennas on Silicon Substrates

Leonetta Baldassarre,[†,‡,#] Emilie Sakat,[§,#] Jacopo Frigerio,[∥] Antonio Samarelli,[⊥] Kevin Gallacher,[⊥] Eugenio Calandrini,[†] Giovanni Isella,[∥] Douglas J. Paul,[⊥] Michele Ortolani,[†] and Paolo Biagioni*[,§]

[†]Dipartimento di Fisica, Università di Roma "La Sapienza", Piazzale Aldo Moro 5, I-00185 Roma, Italy

[‡]Center for Life Nano Science@Sapienza, Istituto Italiano di Tecnologia, Viale Regina Elena 291, I-00161 Roma, Italy

[§]Dipartimento di Fisica, Politecnico di Milano, Piazza Leonardo da Vinci 32, I-20133 Milano, Italy

[∥]LNESS, Dipartimento di Fisica del Politecnico di Milano, polo di Como, via Anzani 42, I-22100 Como, Italy

[⊥]School of Engineering, University of Glasgow, Rankine Building, Oakfield Avenue, Glasgow G12 8LT, U.K.

Supporting Information

ABSTRACT: Midinfrared plasmonic sensing allows the direct targeting of unique vibrational fingerprints of molecules. While gold has been used almost exclusively so far, recent research has focused on semiconductors with the potential to revolutionize plasmonic devices. We fabricate antennas out of heavily doped Ge films epitaxially grown on Si wafers and demonstrate up to 2 orders of magnitude signal enhancement for the molecules located in the antenna hot spots compared to those located on a bare silicon substrate. Our results set a new path toward integration of plasmonic sensors with the ubiquitous CMOS platform.

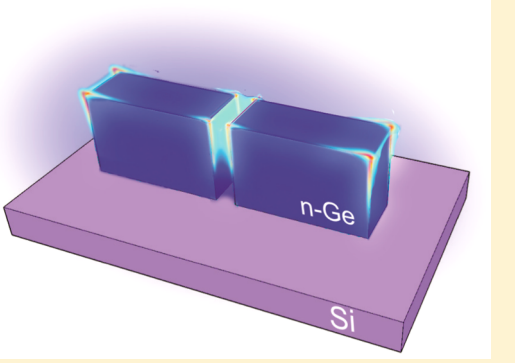

KEYWORDS: *Silicon technology, plasmonics, mid-infrared spectroscopy, explosives detection*

Localized plasmon resonances are nowadays recognized as one of the most powerful mechanisms to boost the interaction between light and matter at the nanoscale. In this frame, recent plasmonic research has searched for novel material platforms, which can improve the quality and integrability of plasmonic interfaces and devices.[1] The choice of the material can impact the crystalline and nanofabrication quality of the device, the spectral range of operation, and the amount of loss. The crucial issue for the future use of plasmonics in everyday applications, however, is the integration with the Si-complementary metal-oxide semiconductor (CMOS) technology process. This is difficult to foresee using the most common metal in plasmonics, gold, due to it being a deep level impurity and a fast diffuser, which is incompatible with silicon technology. Among all applications of plasmonics, molecular sensing has already made its way to the market. Plasmonic sensors can be based on refractive index variations at the metal surface,[2,3] on the local enhancement of the electric field for Raman spectroscopy,[4,5] or on the modification of the engineered transmitted or reflected wavefront in antennas by a resonant molecular vibration in the mid-infrared (IR).[4,6−16] In the past few years the latter approach, mainly pursued with the nanofabrication of gold antennas, led to reported signal enhancements exceeding 3 orders of magnitude for the material located in the antenna hot spots compared to the material outside the hotspots.

While metals are the most natural choice for visible and near-IR plasmonics, it has been suggested that heavily doped semiconductors (i.e., degenerately doped to be metallic) could replace and, possibly, outperform metals in the mid-IR frequency range.[1,14−25] The envisioned advantages for plasmonic device design include (i) the low absolute values of the dielectric constant in the mid-IR, strictly resembling that of metals in the visible and near-IR range but without the detrimental effect of interband transition losses, (ii) the high material quality, thanks to single-crystalline epitaxial growth, (iii) in the case of foundry-compatible group-IV semiconductors like Si and Ge, the potential for on-chip integration of antennas, detectors and readout electronics, all fabricated in a single cost-effective silicon foundry manufacturing process, and (iv) the possibility of active electrical and/or optical tuning of the plasmonic effects by the control of the doping level. The onset of the plasmonic behavior of a conducting material is marked by the so-called plasma frequency ω_p, i.e., the frequency below which the real part of the dielectric constant of the

Received: May 12, 2015
Revised: October 8, 2015
Published: October 12, 2015

DOI: 10.1021/acs.nanolett.5b03247
Nano Lett. 2015, 15, 7225−7231

material becomes negative. Standard doping of semiconductors usually sets ω_p in the far-IR, while entering the mid-IR range requires high doping levels, n up to $10^{19}-10^{20}$ cm^{-3} according to the scaling law $\omega_p \propto (n/m_e)^{1/2}$, m_e being the electron effective mass.

In particular, the development of a plasmonic platform for molecular sensing based on group-IV semiconductors[20−25] could have a dramatic impact on chemical or biological laboratory applications because it could lead to the automation of surface-enhanced IR absorption spectroscopy (SEIRA)[26] by exploiting readily and massively available disposable substrates with integrated readout produced by standard silicon foundry processes. In the long term, semiconductor plasmonic integration could lead to low-cost, compact, and efficient lab-on-a-chip devices for in situ medical diagnostics, environmental monitoring in addition to safety and security sensing. Also, while the performance of semiconductor plasmonic antennas may not be the highest among all possible materials due to unavoidable losses in heavily doped materials, the ability to integrate readout electronics and reference standards close to the detectors may be key to optimize the sensitivity, specificity, and speed of the full sensor system, as has already been demonstrated, e.g., in the development of CMOS single photon detector arrays.[27]

In the past decade epitaxial Ge on Si has become a key technology for silicon photonics due to its demonstrated compatibility with the CMOS technology.[28−30] Band engineering and doping have already allowed for the demonstration of high-performance Ge photodiodes,[31] optical modulators,[32,33] prototype near-IR and far-IR LEDs and laser diodes,[34−36] and integrated systems.[37] Intrinsic Ge is also considered one of the best candidates for dielectric waveguides in the mid-IR range of interest for molecular sensing (wavelengths $\lambda \approx 20$ to 4 μm, or frequency $\omega \approx 500$ to 2500 cm^{-1}).[38,39] The preference of Ge over Si is due to negligible absorption losses compared to Si,[30] which instead features relatively strong IR-active transitions in the 400−1700 cm^{-1} range related to the presence of in-gap defect states. Such Si dipole-active impurity states result in a large number of narrow absorption lines that may overlap to the weak molecular signals of surface-enhanced sensors and complicate their interpretation.[40] Ge, on the other side, displays no impurity absorption lines in the 100−2000 cm^{-1} range, and therefore, it is commonly employed for thick mid-IR optical elements such as lenses and prisms. For applications in mid-IR plasmonics, in particular, Ge has been rarely if at all been used despite the appealing perspective of combining infrared spectroscopy with CMOS integration. When compared with Si, it has the advantage of a smaller electron effective mass ($m_e \approx 0.12$ for n-type Ge and $m_e \approx 0.26$ for n-type Si), which widens the range of applications of plasmonic sensing (allowing for higher ω_p) for a given doping level. This is especially relevant because of the technological issues in achieving extremely high doping levels and because plasmonic losses in doped semiconductors are also influenced by free-carrier scattering by charged impurities, thereby favoring materials that can achieve higher plasma frequencies for a given doping level.

In this work we grow epitaxial Ge films on standard Si wafers using the low-energy plasma-enhanced chemical vapor deposition (LEPECVD, see Supporting Information, Section A) method[41,42] and exploit phosphorus as the donor to achieve a doping level $n \approx 2.3 \times 10^{19}$ cm^{-3}, thus setting $\omega_p \approx 1000$ cm^{-1} (~10 μm wavelength). Micrometer-sized antennas are fabricated out of the epitaxial Ge material by electron-beam lithography and reactive ion etching processes and are characterized by Fourier-transform IR (FTIR) spectroscopy demonstrating localized plasmon resonances in the 400−900 cm^{-1} range. Finally, the fabricated devices are used for plasmon-enhanced sensing experiments, detecting the vibrational fingerprints of thin molecular films and liquids and demonstrating signal enhancements of up to 2 orders of magnitude when the target materials are located at the antenna hotspots.

In order to design the antenna samples, we employ frequency- and time-domain simulations (see Supporting Information, Section A). The dielectric constant of the Ge material for simulations is obtained by numerical fitting of the reflection and transmission FTIR data obtained from unpatterned Ge films in the entire infrared range (see Supporting Information, Section B). The investigated antenna designs, demonstrated in Figure 1, have fixed thickness and

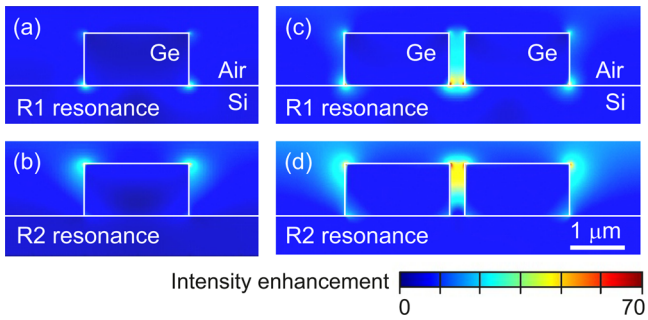

Figure 1. Field intensity distribution (squared modulus of the electric field) in the resonant Ge antennas: the simulated near-field intensity enhancement associated with the excitation of the localized plasmon modes labeled as R1 and R2 in the single-arm gapless antennas (a,b) and the double-arm gap antennas (c,d). All maps are calculated at the respective near-field resonance frequency. Each antenna arm is 2 μm long, and the gap is 300 nm.

width of the order of 1 μm (i.e., comparable with the skin depth of the doped Ge in the 400−900 cm^{-1} range) and a range of arm lengths L varying from 1 to 4 μm (see Supporting Information, Section C). We considered both single-arm (gapless) and double-arm (gap) antennas. The simulations reveal the existence of two longitudinal antenna resonances related to two distinct plasmonic modes propagating along the antenna arms. The first mode ("substrate-like", labeled as R1) lies in the 300−500 cm^{-1} range with the hotspots located at the Si/Ge interface, while the second mode ("air-like", R2) lies in the 800−900 cm^{-1} range with hotspots at the upper antenna edges toward the air half-space. Field intensity maps of the two modes at their respective near-field resonance frequencies are presented in Figure 1. It should be stressed here that a slight spectral shift occurs between the near-field and far-field resonances of the investigated antennas (see Supporting Information, Section C), which is common for lossy plasmonic materials.[43] The electromagnetic origin of the two modes is the same in single-arm and double-arm antennas. The presence of the gap, however, affects the local intensity distribution, further boosting the enhancement and confinement of the field. The evidence for these two modes has already been reported in the literature.[17−19] In particular, the air-like R2 mode is the most promising mode for sensing applications because (i) the fields are located toward the air half-space and therefore interact

DOI: 10.1021/acs.nanolett.5b03247
Nano Lett. 2015, 15, 7225−7231

more effectively with the molecules to be detected and (ii) the higher frequency compared to R1 is an advantage in view of the inherent difficulty in growing high-quality semiconductor materials with heavy doping and therefore with high plasma frequency.

A representative scanning electron microscopy (SEM) image of a fabricated gap antenna sample is presented in Figure 2a. The gap between the two arms is 300 nm, while the period for the array is large enough to avoid significant near-field interactions between neighboring antennas. The samples are characterized by FTIR spectroscopy, measuring both the transmission and reflection spectra at normal incidence with the electric field linearly polarized along the antenna axis. In the perspective of an integrated CMOS sensing device, however, it is worth discussing the antenna signatures in reflection geometry. Indeed the use of an optical scheme based on reflection instead of transmission is key in developing realistic mid-IR chemical sensing devices as it can be coupled to, e.g., a sensing chip equipped with microfluidics (aqueous solutions are not transparent at mid-IR frequencies).[6] Additionally, the measured transmission suffers from light diffusion coming from the backside roughness[17] and from absorptions in a thick Si substrate with a standard concentration of impurities.[30]

Figure 2b–d demonstrates a comparison between the calculated and measured reflection and extinction spectra of three different antennas, namely, two single-arm antennas with lengths L = 2.0 and 3.0 μm, respectively, and one gap antenna with L = 2.0 μm for the individual antenna arms. In order to extract the antenna response, we demonstrate in Figure 2b–d a normalized extinction $E_{norm} = 1 - (T_{ant}/T_{Si})$, with T_{ant} and T_{Si} being the transmission spectra acquired from the antenna sample and from the bare Si substrate, respectively, and the reflection $R = (R_{ant}/R_{Au})$, with R_{ant} and R_{Au} being the reflection spectra acquired from the antenna sample and from a bare Au mirror, respectively. The experimental results (solid lines in the left column) clearly display two resonances corresponding to the R1 and R2 modes described before. Noticeably, the two spectral features are not present in geometrically identical antennas fabricated out of lightly doped Ge on Si ($n \approx 1.5 \times 10^{17}$ cm^{-3} and $\omega_p < 100$ cm^{-1}, dashed lines), which acts as a purely dielectric material in the investigated frequency range, thus demonstrating that the resonances observed in the doped samples are due to localized plasmons of the conduction electrons. This is also in agreement with the redshift of the resonances with increasing arm length (compare the spectra of 2 and 3 μm single-arm antennas in Figure 2b,d), as expected for plasmonic antennas.[44] We have also verified that the two strong resonant features disappear when the excitation electric field is oriented perpendicular to the antenna axis and only the much weaker transverse resonances are excited (see Supporting Information, Section E).

The simulated spectra at normal incidence for the investigated antenna samples, also displayed in Figure 2b–d, are in excellent agreement with the experiments, with small discrepancies that can be attributed mainly to uncertainties in the value of the dielectric constant. Calculations have also been performed to confirm that no collective behavior contributes to the R1 and R2 resonance mechanisms. The spectral positions of the resonances have been found to be largely independent of the incidence angle of excitation and periodicity of the array (see Supporting Information, Sections C and E), which highlights the localized character of the two resonances and confirms that we are indeed addressing the plasmonic response

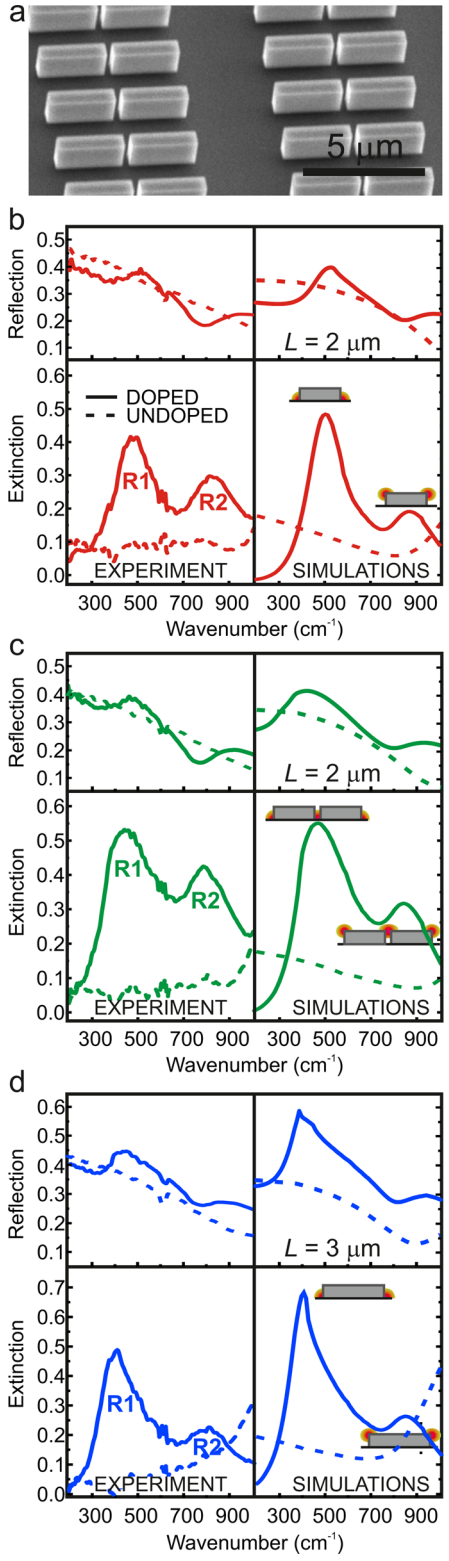

Figure 2. Demonstration of mid-IR plasmon resonances in Ge antennas: (a) a representative SEM image of a Ge antenna sample. (b–d) Experimental and simulated reflection and extinction spectra for single-arm antennas with L = 2.0 μm length (b), gap antennas with L = 2.0 μm arm length (c), and single-arm antennas with L = 3.0 μm length (d). The solid lines refer to doped plasmonic antennas, and the dashed lines refer to undoped nonplasmonic antennas. For the sake of clarity, all the transmission spectra from the undoped antennas have been rescaled by 0.8 before the calculation of the normalized extinction ratio.

DOI: 10.1021/acs.nanolett.5b03247
Nano Lett. 2015, 15, 7225–7231

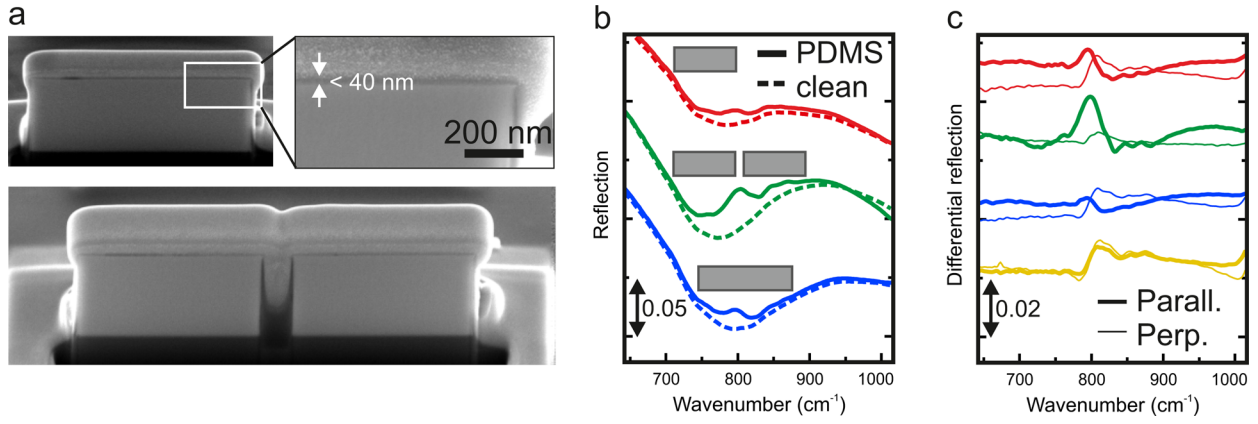

Figure 3. Solid-state sensing of a thin PDMS layer: (a) cross-sectional SEM images of the PDMS-covered antennas, obtained after deposition of a Pt overlayer with the slice-and-view technique in a dual-beam apparatus. The length of the single-arm antenna is 3 μm, while individual arms of the gap antenna are 2 μm long. (b) The experimental reflection spectra acquired after PDMS spin coating on the three antenna samples (solid lines) and reference spectra from the clean samples (dashed lines); the spectra have been translated vertically for the sake of clarity. (c) The difference spectra obtained after subtraction of the spectra from antennas coated with AZ-5214; the spectra have been translated vertically for the sake of clarity. Thicker lines correspond to polarization parallel to the antenna axis, thinner lines to perpendicular polarization. The color coding is the same as in panel b, and the yellow lines refer to an undoped antenna sample.

of individual antennas. This paves the way toward engineered devices where individual semiconductor antennas, each one with a specific spectral response, are integrated on the same miniaturized silicon chip. Only in the case of Figure 2d, the reader should notice that the asymmetric shape of the peak around 400 cm^{-1} is due to the occurrence of a Rayleigh anomaly, as thoroughly discussed in the Supporting Information (Section C).

With this understanding of the plasmonic properties of the antenna samples, we have explored the potential for sensing using a reflection geometry, which is best suited for on-chip integrated antennas. We have exploited the R2 resonance for the sensing of both thin solid-state layers and liquid-phase droplets of substances with vibrational fingerprints in the spectral window covered by R2.

In a first experiment (see Figure 3), we have coated the same antennas of Figure 2 with a polydimethylsiloxane (PDMS) layer, which features a vibrational absorption resonance at 800 cm^{-1} (see Supporting Information, Section F) due to the Si−C bond stretching modes. This absorption line matches very well the spectral position of the R2 near-field resonance of the antennas, as demonstrated in Figure S4 of the Supporting Information. By spin-coating the highly diluted PDMS and further curing, we obtained a PDMS thickness below 40 nm, as demonstrated in the SEM cross-section images of the PDMS-coated Ge antennas (obtained by the slice-and-view technique with a dual electron and ion beam apparatus) in Figure 3a. Reflection spectra for the antenna samples are displayed in Figure 3b. A comparison between the reflection spectra of the clean samples (dashed lines) and of the spin-coated samples (solid lines) reveals that the PDMS layer induces two changes in the spectra: a slight redshift of the plasmonic resonance, due to the increased refractive index in the antenna surroundings, and the appearance of an asymmetric spectral line around 800 cm^{-1}. Such Fano-like interferences have already been the subject of extensive studies in the literature.[7,12,45−47] In order to provide further support to the actual interaction between the PDMS vibrational resonances and the plasmonic field of the antennas, we also acquired reflection spectra after covering the antennas with a polymer (AZ-5214) having similar refractive index to PDMS but very weak absorption features in the spectral window under consideration (see also Section G of the Supporting Information). In this way, we obtained correctly red-shifted reference antenna spectra that can be used for background subtraction from those obtained from PDMS-covered antennas. Through this experiment, we are able to demonstrate (see Figure 3c) that the line-shape around 800 cm^{-1} is completely different for parallel and perpendicular polarization and that the line-shape obtained for perpendicular polarization is similar to the one obtained from nominally undoped antenna samples. This observation clearly highlights the electromagnetic coupling between PDMS and the longitudinal plasmon resonances.

We also calculated (see Section H of the Supporting Information) the ratio between the experimental spectra acquired from PDMS-coated antennas with parallel and perpendicular polarization, both for the doped and undoped samples. Noticeably, the 800 cm^{-1} vibrational feature from PDMS completely disappears in the undoped antennas after such normalization, meaning that no PDMS-antenna interaction is taking place irrespective of the field polarization. On the other side, a clear Fano-like line survives when the same normalization is performed for doped antenna samples, again unambiguously highlighting the role of longitudinal localized plasmon resonances.

We now focus our attention on the gap antennas, which display the strongest field enhancement. Figure 4a (left panel) provides a comparison between the spectra acquired with the polarization parallel (solid line) and perpendicular (dashed line) to the antenna axis. The experimental results compare well with those from numerical simulations, also presented in Figure 4a (right panel). It should be noted here that, as observed in the SEM image in Figure 3a, the PDMS does not conformally cover the antenna gap, rather a PDMS meniscus is created due to the surface tension. This is fully taken into account in the simulations. Clearly, since the hotspots related to the R2 resonance are located right at the upper antenna edges, where the PDMS adheres almost perfectly to the antenna, this does not compromise the sensing experiment. The use of an antenna resonance with the associated field hotspots located in the air half space is therefore confirmed to be an interesting

DOI: 10.1021/acs.nanolett.5b03247
Nano Lett. 2015, 15, 7225−7231

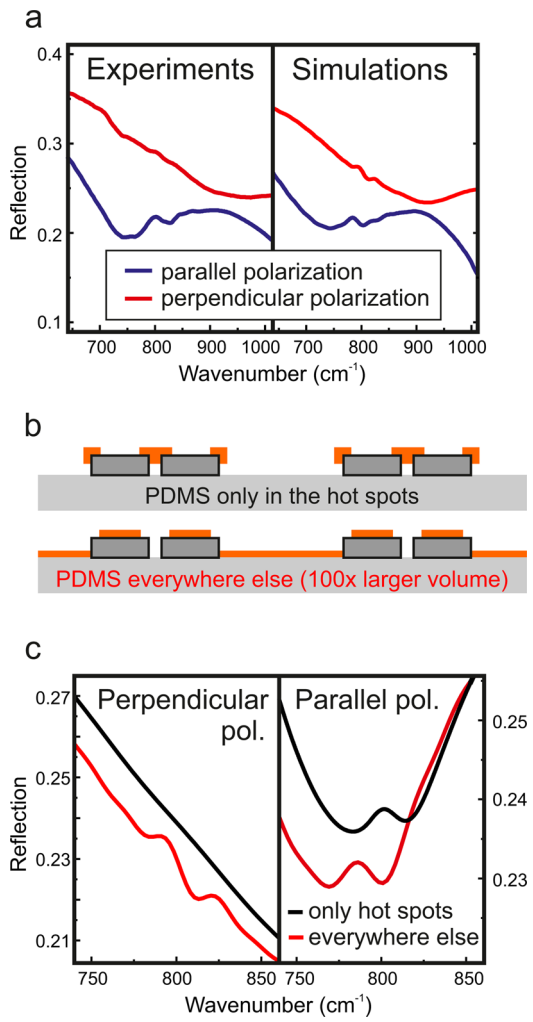

Figure 4. (a) Experimental (left panel) and simulated (right panel) reflection spectra from the PDMS-covered gap antenna sample, obtained with the field polarization parallel (blue line) or perpendicular (red line) to the antenna axis. The simulated spectra have been translated vertically for the sake of clarity. (b) Sketch of the PDMS distribution in the simulations demonstrated in panel c. (c) Simulations of reflection spectra highlighting the individual contributions coming from the antenna hot spots (black lines) and from everywhere else (red lines), for light with the polarization perpendicular to the antenna axis (left panel) and parallel to the antenna axis (right panel).

feature that simplifies the requirements for analyte delivery into the antenna gap.

In order to further clarify the role of the plasmonic hotspots, we also ran two separate simulations (see Figure 4b), the first one with PDMS placed only in the hotspots (black lines in Figure 4c) and the second one with the PDMS coating everywhere except in the hotspots (red lines in Figure 4c). The total PDMS volume in the former simulation is about 100 times smaller than in the latter. In the left panel of Figure 4c, for the perpendicular field polarization and PDMS only in the hotspots, the simulations do not display any detectable sign of the PDMS vibrational mode at 800 cm^{-1}. On the contrary, when the PDMS coating is everywhere except in the hotspots the vibrational mode is clearly visible. This behavior is at complete variance with what is observed in the right panel of Figure 4c, i.e., for electric field polarization parallel to the antenna axis. Therein, one clearly observes that the PDMS absorption line is visible in both simulations (PDMS only in the hot spots and PDMS everywhere else). Indeed, while having a different line-shape because of the interaction with the plasmonic resonance when the PDMS is in the hotspots, the two vibrational features have roughly the same spectral weight, indicating that the respective perturbations to the antenna spectrum have similar strengths. Since the simulated PDMS volume in the hotspots only is about 100 times smaller than outside the hotspots, we estimate an enhancement factor of up to 2 orders of magnitude for the optical signal generated by the PDMS in the hotspots, compared to the PDMS outside the hotspots.

It is important here to stress that the experimentally observed line shape (Figure 4a, left panel) is interpreted as the far-field interference of the two contributions outlined in Figure 4c for the parallel polarization (black and red lines in the right panel). Their individual line shapes are determined by two mechanisms: on the one side, the reflection geometry is known to produce Fano-like features because of the interference between the light interacting with the PDMS layer and that directly reflected by the substrate.[46] On the other side, we have the interaction between the PDMS and the antenna resonance in the hot spots. The situation is further complicated by the presence of shoulders and side peaks in the PDMS vibrational feature around 800 cm^{-1} (see Section F of the Supporting Information). The overall interference process between the two contributions in Figure 4c, each one carrying its own specific phase, is therefore not easy to deconvolve, yet it is accurately described and predicted by full-wave simulations in Figure 4a (right panel). Incidentally, one may notice that the estimated two-order-of-magnitude enhancement in the sensing experiment is slightly larger than the average local intensity enhancement expected in the antenna hot spots (see Figure 1). This must likely be ascribed to small uncertainties in the dielectric description of the Ge/PDMS system and in the evaluation of the enhancement for the sensing experiment.

Finally, we applied Ge plasmonic antennas to the sensing of chloroethyl methyl sulfide (CEMS), a transparent liquid with mass density similar to that of water that is a simulant of common explosive materials and cannot easily be distinguished from harmless liquids, except by spectroscopy. During the experiment (Figure 5a), the decrease in thickness of the droplet due to evaporation was monitored with the same spectroscopy setup used for the sensing demonstration by continuously acquiring fast FTIR spectra every 5 s and by measuring the period of the Fabry–Pérot interference fringes in the near-IR. When the droplet thickness was estimated to be below 2 μm, longer FTIR spectra with higher signal-to-noise ratios were acquired. Due to the large volatility of the investigated substances, we are not able to quantitatively assess the exact fraction of liquid inside and outside the hotspots, to provide a precise value of the signal enhancement due to the antennas. Figure 5b demonstrates the IR absorption fingerprint spectrum of the pure substance (gray line), obtained in transmission geometry with a 20-μm-thick IR cuvette. A strong vibrational doublet appears at 690–720 cm^{-1}, i.e., below the plasma frequency of our material in the region of plasmonic behavior, while a second fingerprint of similar vibrational absorption strength appears around 1430 cm^{-1} in the region of dielectric behavior of the Ge, i.e., above the plasma frequency. In Figure 5c we also demonstrate the spectrum of the doped Ge antennas covered with a droplet of CEMS (red line) superimposed onto the spectrum of the clean antenna sample (black dashed line).

DOI: 10.1021/acs.nanolett.5b03247
Nano Lett. 2015, 15, 7225–7231

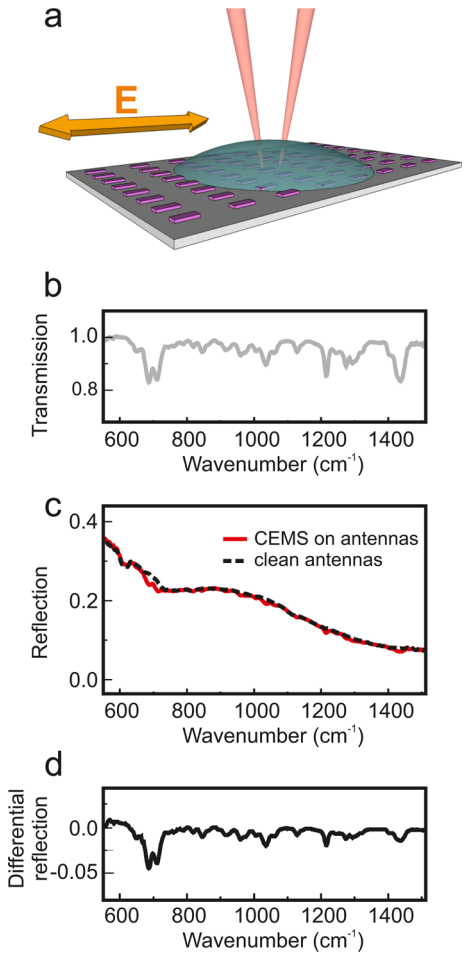

Figure 5. Hazardous liquid sensing experiment: (a) a sketch of the reflection sensing geometry; (b) the transmission spectrum of pure CEMS in a 20 μm thick standard IR cuvette; (c) the reflection spectrum for a CEMS-covered antenna array (red line) and the reflection spectrum from the clean antenna array (black dashed line); and (d) the difference between the two spectra in panel c.

By taking the difference between these two spectra, the vibrational molecular fingerprint of CEMS is clearly recovered (Figure 5d). One can notice, however, that the relative spectral weight of the doublet at 690−720 cm^{-1} compared to the feature at 1430 cm^{-1} in Figure 5d is stronger than in the bare liquid material of Figure 5b, thus qualitatively pointing toward a signal enhancement provided by the plasmonic antenna response below the plasma frequency of our material (see also Supporting Information, Section J).

In conclusion, we have introduced a novel all-group-IV semiconductor material platform for mid-IR plasmonics, based on heavily doped Ge epitaxially grown on standard Si wafers. We demonstrated localized plasmon resonances in Ge antennas and exploited the fabricated devices for sensing experiments based on the resonant detection of molecular vibrational fingerprints of both condensed-phase and liquid-phase analytes. While the present work demonstrates doping levels of about 2.3×10^{19} cm^{-3}, reaching a plasma frequency around 1000 cm^{-1}, the whole relevant fingerprint region extending roughly up to 1800 cm^{-1} can be in principle reached given the high solubility of P dopants in Ge,[49] and the recent efforts to demonstrate carrier densities of the order of 10^{20} cm^{-3} in n-type Ge.[50] Enhancement factors of up to 2 orders of magnitude for the material located in the antenna hotspots have been obtained in the present work. Although the demonstrated enhancement is still below that obtained with state-of-the-art Au antennas[8,13] and the accessible wavelength range is slightly narrower than what has been obtained with III−V compound semiconductor antennas,[17] the demonstrated Ge antennas are compatible with silicon CMOS technology, which can in turn be used to build intelligent sensor networks with a very large number of sensing elements at a far lower cost. As in most direct CMOS applications, the performance of the single sensor must be traded for the number of identical sensors with integrated readout electronics that can be realized, when compared with optimized stand-alone antennas. The developed technology holds great promise for the realization of CMOS-compatible mid-IR devices for substance-specific molecular sensing. The field enhancement in the plasmonic hotspots may also find applications in other fields where the on-chip integration of plasmonics with electronics is expected to play a key role, e.g., in IR imaging, light detection, and energy harvesting.

■ ASSOCIATED CONTENT

Supporting Information

The Supporting Information is available free of charge on the ACS Publications website at DOI: 10.1021/acs.nanolett.5b03247.

Methods; dielectric constant extraction of the unpatterned Ge material; electromagnetic simulations; geometrical details of the samples investigated in the main manuscript; detailed analysis of the infrared spectra of the antenna arrays; absorbance spectra of PDMS and CEMS; PDMS sensing, comparison with a weakly absorbing polymer; PDMS sensing, comparison with undoped antennas; PDMS sensing, role of the R1 resonance; and CEMS sensing, simulated near-field enhancement (PDF)

■ AUTHOR INFORMATION

Corresponding Author

*E-mail: paolo.biagioni@polimi.it.

Author Contributions

#These authors contributed equally to this work. J.F. and G.I. performed the growth of heavily doped Ge on Si. E.S. and P.B. performed the numerical simulations. A.S., K.G., and D.J.P. fabricated the devices. L.B., E.C., and M.O. performed the FTIR characterization. P.B., M.O., and D.J.P. coordinated the work and wrote the draft of the manuscript. All authors contributed extensively to the analysis and discussion of the results and to the revision of the manuscript.

Funding

The research leading to these results has received funding from the European Union's Seventh Framework Programme under grant agreement no. 613055.

Notes

The authors declare no competing financial interest.

■ ACKNOWLEDGMENTS

The authors would like to thank the staff of the James Watt Nanofabrication Centre for help in fabricating the samples and A. De Ninno and A. Notargiacomo of CNR-IFN-Rome for the PDMS film preparation and inspection by focused ion beam. Fruitful discussions with M. Bollani, D. Brida, M. Celebrano, S.

DOI: 10.1021/acs.nanolett.5b03247
Nano Lett. 2015, 15, 7225−7231

Collin, L. Duò, M. Finazzi, and P. Ghenuche are gratefully acknowledged.

REFERENCES

(1) Boltasseva, A.; Atwater, H. A. *Science* **2011**, *331*, 290−291.
(2) Liu, N.; Tang, M. L.; Hentschel, M.; Giessen, H.; Alivisatos, A. P. *Nat. Mater.* **2011**, *10*, 631−636.
(3) Svedendahl, M.; Chen, S.; Dmitriev, A.; Käll, M. *Nano Lett.* **2009**, *9*, 4428−4433.
(4) D'Andrea, C.; Bochterle, J.; Toma, A.; Huck, Ch.; Neubrech, F.; Messina, E.; Fazio, B.; Maragò, O. M.; Di Fabrizio, E.; de La Chapelle, M. L.; Gucciardi, P. G.; Pucci, A. *ACS Nano* **2013**, *7*, 3522−3531.
(5) De Angelis, F.; Das, G.; Candeloro, P.; Patrini, M.; Galli, M.; Bek, A.; Lazzarino, M.; Maksymov, I.; Liberale, C.; Andreani, L. C.; Di Fabrizio, E. *Nat. Nanotechnol.* **2010**, *5*, 67−72.
(6) Adato, R.; Altug, H. *Nat. Commun.* **2013**, *4*, 2154−2163.
(7) Adato, R.; Artar, A.; Erramilli, S.; Altug, H. *Nano Lett.* **2013**, *13*, 2584−2591.
(8) Adato, R.; Yanik, A. A.; Amsden, J. J.; Kaplan, D. L.; Omenetto, F. G.; Hong, M. K.; Erramilli, S.; Altug, H. *Proc. Natl. Acad. Sci. U. S. A.* **2009**, *106*, 19227−19232.
(9) Brown, L. V.; Zhao, K.; King, N.; Sobhani, H.; Nordlander, P.; Halas, N. J. *J. Am. Chem. Soc.* **2013**, *135*, 3688−3695.
(10) Limaj, O.; Lupi, S.; Mattioli, F.; Leoni, R.; Ortolani, M. *Appl. Phys. Lett.* **2011**, *98*, 091902.
(11) Neubrech, F.; Pucci, A.; Cornelius, Th. W.; Karim, S.; García-Etxarri, A.; Aizpurua, J. *Phys. Rev. Lett.* **2008**, *101*, 157403.
(12) Wu, C.; Khanikaev, A. B.; Adato, R.; Arju, N.; Yanik, A. A.; Altug, H.; Shvets, G. *Nat. Mater.* **2011**, *11*, 69−75.
(13) Brown, L. V.; Yang, X.; Zhao, K.; Zheng, B. Y.; Nordlander, P.; Halas, N. J. *Nano Lett.* **2015**, *15*, 1272−1280.
(14) Naik, G. V.; Shalaev, V. M.; Boltasseva, A. *Adv. Mater.* **2013**, *25*, 3264−3294.
(15) Caldwell, J. D.; Lindsay, L.; Giannini, V.; Vurgaftman, I.; Reinecke, Th. L.; Maier, S. A.; Glembocki, O. J. *Nanophotonics* **2015**, *4*, 44−68.
(16) Law, S.; Podolskiy, V.; Wasserman, D. *Nanophotonics* **2013**, *2*, 103−130.
(17) Law, S.; Yu, L.; Rosenberg, A.; Wasserman, D. *Nano Lett.* **2013**, *13*, 4569−4574.
(18) Wang, T.; Nguyen, V. H.; Buchenauer, A.; Schnakenberg, U.; Taubner, Th. *Opt. Express* **2013**, *21*, 9005−9010.
(19) N'Tsame Guilengui, V.; Cerutti, L.; Rodriguez, J.-B.; Tournié, E.; Taliercio, T. *Appl. Phys. Lett.* **2012**, *101*, 161113.
(20) Ginn, J. C.; Jarecky, R. L., Jr.; Shaner, E. A.; Davids, P. S. *J. Appl. Phys.* **2011**, *110*, 043110.
(21) Shahzad, M.; Medhi, G.; Peale, R. E.; Buchwald, W. R.; Cleary, J. W.; Soref, R.; Boreman, G. D.; Edwards, O. *J. Appl. Phys.* **2011**, *110*, 123105.
(22) Law, S.; Adams, D. C.; Taylor, A. M.; Wasserman, D. *Opt. Express* **2012**, *20*, 12155−12165.
(23) Hoffman, A. J.; Alekseyev, L.; Howard, S. S.; Franz, K. J.; Wasserman, D.; Podolskiy, V. A.; Narimanov, E. E.; Sivco, D. L.; Gmachl, C. *Nat. Mater.* **2007**, *6*, 946−950.
(24) Soref, R.; Hendrickson, J.; Cleary, J. W. *Opt. Express* **2012**, *20*, 3814−3824.
(25) Biagioni, P.; Frigerio, J.; Samarelli, A.; Gallacher, K.; Baldassarre, L.; Sakat, E.; Calandrini, E.; Millar, R. W.; Giliberti, V.; Isella, G.; Paul, D. J.; Ortolani, M. *J. Nanophotonics* **2015**, *9*, 093789.
(26) Schwarz, B.; Reininger, P.; Ristanić, D.; Detz, H.; Andrews, A. M.; Schrenk, W.; Strasser, G. *Nat. Commun.* **2014**, *5*, 4085−4091.
(27) Palubiak, D. P.; Deen, M. J. *IEEE J. Sel. Top. Quantum Electron.* **2014**, *20*, 6000718.
(28) Paul, D. J. *Electron. Lett.* **2009**, *45*, 582−584.
(29) Soref, R. *Silicon* **2010**, *2*, 1−6.
(30) Soref, R. *Nat. Photonics* **2010**, *4*, 495−497.
(31) Warburton, R. E.; Intermite, G.; Myronov, M.; Alfred, P.; Leadley, D. R.; Gallacher, K.; Paul, D. J.; Pilgrim, N. K.; Lever, L. J. M.; Ikonic, Z.; Kelsall, R. W.; Huante-Ceron, E.; Knights, A. P.; Buller, G. S. *IEEE Trans. Electron Devices* **2013**, *60*, 3807−3813.
(32) Rouifed, M. S.; Chaisakul, P.; Marris-Morini, D.; Frigerio, J.; Isella, G.; Chrastina, D.; Edmond, S.; Le Roux, X.; Coudevylle, J.-R.; Vivien, L. *Opt. Lett.* **2012**, *37*, 3960−3962.
(33) Dumas, D. C. S.; Gallacher, K.; Rhead, S.; Myronov, M.; Leadley, D. R.; Paul, D. J. *Opt. Express* **2014**, *22*, 19284−19292.
(34) Liu, J.; Sun, X.; Camacho-Aguilera, R.; Kimerling, L. C.; Michel, J. *Opt. Lett.* **2010**, *35*, 679−681.
(35) Camacho-Aguilera, R. E.; Cai, Y.; Patel, N.; Bessette, J. T.; Romagnoli, M.; Kimerling, L. C.; Michel, J. *Opt. Express* **2012**, *20*, 11316−11320.
(36) Matmon, G.; Paul, D. J.; Lever, L.; Califano, M.; Ikonić, Z.; Kelsall, R. W.; Zhang, J.; Chrastina, D.; Isella, G.; von Känel, H.; Müller, E.; Neels, A. *J. Appl. Phys.* **2010**, *107*, 053109.
(37) Chaisakul, P.; Marris-Morini, D.; Frigerio, J.; Chrastina, D.; Rouifed, M.-S.; Cecchi, S.; Crozat, P.; Isella, G.; Vivien, L. *Nat. Photonics* **2014**, *8*, 482−488.
(38) Malik, A.; Dwivedi, S.; Van Landschoot, L.; Muneeb, M.; Shimura, Y.; Lepage, G.; Van Campenhout, J.; Vanherle, W.; Van Opstal, T.; Loo, R.; Roelkens, K. *Opt. Express* **2014**, *22*, 28479−28488.
(39) Chang, Y.-C.; Paeder, V.; Hvozdara, L.; Hartmann, J.-M.; Herzig, H. P. *Opt. Lett.* **2012**, *37*, 2883−2885.
(40) Silicon. www.tydexoptics.com/materials1/for_transmission_optics/silicon (accessed August 13, 2015).
(41) Isella, G.; Chrastina, D.; Rössner, B.; Hackbarth, T.; Herzog, H.-J.; König, U.; von Känel, H. *Solid-State Electron.* **2004**, *48*, 1317.
(42) Rosenblad, C.; Deller, H. R.; Dommann, A.; Meyer, T.; Schroeter, P.; von Känel, H. *J. Vac. Sci. Technol., A* **1998**, *16*, 2785−2780.
(43) Zuloaga, J.; Nordlander, P. *Nano Lett.* **2011**, *11*, 1280−1283.
(44) Biagioni, P.; Huang, J.-S.; Hecht, B. *Rep. Prog. Phys.* **2012**, *75*, 024402.
(45) Giannini, V.; Francescato, Y.; Amrania, H.; Phillips, Ch. C.; Maier, S. A. *Nano Lett.* **2011**, *11*, 2835−2840.
(46) Svedendahl, M.; Käll, M. *ACS Nano* **2012**, *6*, 7533−7539.
(47) Luk'yanchuk, B.; Zheludev, N. I.; Maier, S. A.; Halas, N. J.; Nordlander, P.; Giessen, H.; Chong, C. T. *Nat. Mater.* **2010**, *9*, 707−715.
(48) Alonso-González, P.; Albella, P.; Schnell, M.; Chen, J.; Huth, F.; García Etxarri, A.; Casanova, F.; Golmar, F.; Arzubiaga, L.; Hueso, L. E.; Aizpurua, J.; Hillenbrand, R. *Nat. Commun.* **2012**, *3*, 684−690.
(49) Vanhellemont, J.; Simoen, E. *Mater. Sci. Semicond. Process.* **2012**, *15*, 642−655.
(50) Scappucci, G.; Klesse, W. M.; Yeoh, L. A.; Carter, D. J.; Warschkow, O.; Marks, N. A.; Jaeger, D. L.; Capellini, G.; Simmons, M. Y.; Hamilton, A. R. *Sci. Rep.* **2015**, *5*, 12948.

DOI: 10.1021/acs.nanolett.5b03247
Nano Lett. 2015, 15, 7225−7231